

Dynamic Plasmonic Pixels

Nicholas J. Greybush,[†] Kristin Charipar,^{†,ID} Jeffrey A. Geldmeier,[†] Stephen J. Bauman,[‡] Paul Johns,^{†,ID} Jawad Naciri,[†] Nicholas Charipar,[†] Kyoungweon Park,^{§,ID} Richard A. Vaia,^{§,ID} and Jake Fontana^{*,†,ID}

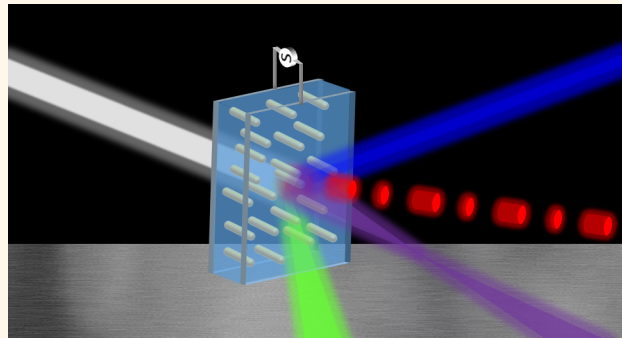
[†]United States Naval Research Laboratory, 4555 Overlook Ave, SW, Washington, DC 20375, United States

[‡]University of Arkansas Fayetteville, 3189 Bell, 1 University of Arkansas, 800 West Dickson, Fayetteville, Arkansas 72701, United States

[§]Air Force Research Laboratory, AFRL 2941 Hobson Way, Wright-Patterson AFB, Ohio 45433, United States

S Supporting Information

ABSTRACT: Information display utilizing plasmonic color generation has recently emerged as an alternative paradigm to traditional printing and display technologies. However, many implementations so far have either presented static pixels with a single display state or rely on relatively slow switching mechanisms such as chemical transformations or liquid crystal transitions. Here, we demonstrate spatial, spectral, and temporal control of light using dynamic plasmonic pixels that function through the electric-field-induced alignment of plasmonic nanorods in organic suspensions. By tailoring the geometry and composition (Au and Au@Ag) of the nanorods, we illustrate light modulation across a significant portion of the visible and infrared spectrum (600–2400 nm). The fast (~30 μ s), reversible nanorod alignment is manifested as distinct color changes, characterized by shifts of observed chromaticity and luminance. Integration into larger device architectures is showcased by the fabrication of a seven-segment numerical indicator. The control of light on demand achieved in these dynamic plasmonic pixels establishes a favorable platform for engineering high-performance optical devices.



KEYWORDS: plasmonic pixel, Au nanorod alignment, color displays, active plasmonics, fast switching speed, core–shell nanorods

An established technology to actively control the properties of light such as the amplitude, phase, and polarization is that of liquid crystal (LC) displays, or more generally, LC spatial light modulators. However, a significant limitation of LC-based devices is their relatively slow switching speeds, on the order of tens of milliseconds for conventional Fréedericksz-transition mechanisms,¹ often resulting in undesirable motion-blur artifacts in displays.^{2,3}

An emerging alternative for improving information displays is the utilization of plasmonic nanomaterials.^{4–8} While approaches incorporating a great diversity of plasmonic materials and geometrical architectures promise to yield vibrant static images,^{9–26} the development of techniques for dynamic plasmonic color display⁷ presents additional challenges. Researchers have applied several schemes to achieve active control of plasmon resonances,²⁷ such as modifying the local dielectric environment of the resonators,^{28–30} mechanically adjusting the coupling within nanostructures,³¹ applying external magnetic fields,^{32,33} and employing chemical and electrochemical switching.^{34–41} Of particular note, many demonstrations incorporate LC materials to achieve light modulation,⁴² either by tuning the refractive index,^{28–30} inducing plasmonic nanocrystal alignment,⁴³ or acting as a

light valve integrated with the plasmonic nanostructure.⁴⁴ However, these approaches still suffer from either slow switching times, small amplitude changes, or narrow wavelength tunability.

We recently proposed the electric-field-induced alignment of gold nanorods (NRs) in organic suspensions as an alternative paradigm to anisotropic LC molecules with the potential for display devices.⁴⁵ A key advantage of these NR suspensions over conventional LC devices is the decrease of switching time by at least 3 orders of magnitude due to the absence of near-neighbor interactions, establishing the effectiveness of this approach for high-performance optical devices with fast switching times.^{46,47}

Here, we demonstrate a dynamic plasmonic pixel that modulates the spatial, temporal, and spectral properties of light on demand. The pixel is composed of a suspension of colloidal NRs orientable by electric fields. We systematically examine the implementation of NRs as plasmonic pixels for visible and infrared (IR) operation. We illustrate the wide tunability of the

Received: January 31, 2019

Accepted: February 22, 2019

Published: February 22, 2019

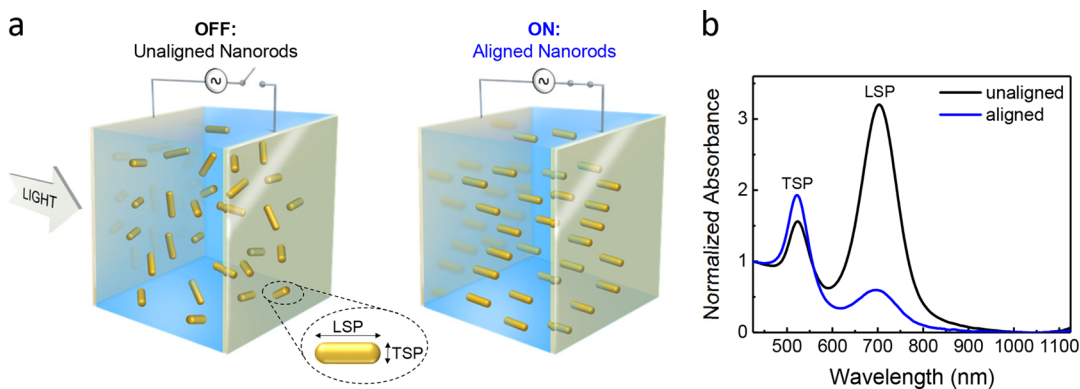


Figure 1. (a) Schematic depiction of the dynamic plasmonic pixel when the applied electric field is OFF (unaligned: 0 V/ μ m) and ON (aligned: 6 V/ μ m). (b) Measured pixel extinction spectra of a suspension of polystyrene-thiol-coated Au NRs in toluene when the applied electric field is OFF (black) and ON (blue). The 60 Hz AC field is applied across a glass capillary of total thickness 0.5 mm and optical path 0.2 mm that contains the NR suspension. The equivalent, unnormalized optical density for a 1 cm path at the LSP resonance peak is approximately 6.5.

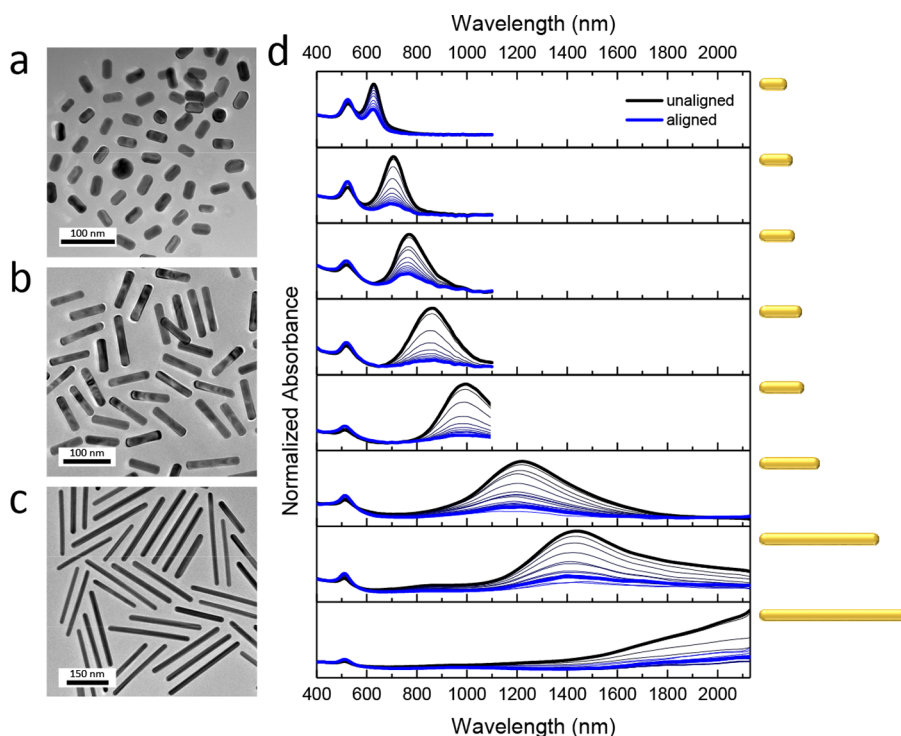


Figure 2. (a–c) TEM images of Au NRs with three different aspect ratios. (d) Measured extinction spectra of eight different aspect ratio polystyrene-thiol-coated Au NRs in toluene in glass capillaries with total thickness of 0.5 mm and optical path length of 0.2 mm as the 60 Hz applied electric field is varied from 0 V/ μ m (unaligned: thick black) to 6 V/ μ m (fully aligned: thick blue). Absorbance is normalized within each panel. The schematics at the right depict the NR aspect ratio associated with each spectrum. The TEM images of (a–c) correspond to the top, fifth, and bottom spectra in (d), respectively.

plasmon resonance wavelength by tailoring both NR geometry and chemical composition. Choosing from the resulting library of NR candidates enables color modulation across a significant portion of perceivable chromaticities, which may facilitate trichromatic color-mixing schemes in compound pixels. Finally, we fabricate a seven-segment numerical indicator, exemplifying the control achievable in our dynamic plasmonic pixel platform.

RESULTS AND DISCUSSION

The dynamic plasmonic pixel is schematically represented in Figure 1a. A suspension of polymer-coated Au NRs in a

nonpolar solvent is placed between two transparent conducting electrodes. NR alignment is achieved by applying a voltage across the electrodes, generating an electric field in the NR suspension and aligning the long axes of the NRs parallel to the applied field direction.^{45,48–55} The optical anisotropy of the individual Au NRs results in a significant modulation of the plasmonic pixel's optical properties upon switching between the OFF (unaligned) and ON (aligned) states.

Upon illumination, each individual plasmonic NR can support collective electron oscillations along its transverse and longitudinal dimensions. These localized surface plasmon

resonances result in enhanced extinction at certain wavelengths of light, as pictured in [Figure 1b](#).

Light polarized along the long axis of a NR induces excitation of the long-wavelength longitudinal surface plasmon (LSP) mode, while orienting the short dimension along the polarization direction excites the short-wavelength transverse surface plasmon (TSP) mode. In a suspension of NRs that are randomly oriented with respect to the incident light, both the LSP and TSP modes of each individual NR are excited. Collecting an extinction spectrum of the entire population averages the individual NR contributions, resulting in an ensemble spectrum that displays both TSP and LSP absorbance peaks ([Figure 1](#), “unaligned”). While for a randomly oriented NR population the ratio of intensity between the two peaks is fixed by the intrinsic oscillator strength of each resonance, the relative proportion of LSP and TSP response can be controlled by inducing NR alignment. If the NRs are each aligned along the direction of light propagation as depicted in [Figure 1a](#), then the LSP mode is at a minimum and the TSP mode at a maximum. This results in suppression of the LSP absorbance peak and enhancement of the transverse peak in the spectrum ([Figure 1b](#), “aligned”). As explored in detail below, this modulation of the ensemble NR extinction spectrum between unaligned and aligned NRs leads to clearly observable changes in the color and brightness of light passing through the NR suspension.

Tailoring the NR dimensions and/or chemical composition enables the operating wavelength to be tuned across a wide spectral range. To demonstrate, we first prepared a series of Au NR samples of fixed composition with eight different aspect ratios ranging from 2.3 to 12.7. Representative transmission electron microscopy (TEM) images of three such NR samples are displayed in [Figure 2a–c](#). By changing the NR dimensions, the position of the LSP wavelength can be varied from ~630 to 2230 nm for the examples shown in [Figure 2d](#). Furthermore, the modulation of the TSP and LSP resonances in the spectra upon NR alignment is consistent across the eight examples pictured.

The applied electric field induces an electric dipole moment in the NRs, which then creates a torque promoting reorientation of the NR long axis along the applied field direction. However, the NRs in suspension also undergo rotational diffusion due to Brownian motion that randomizes the NR orientation. Therefore, the degree of NR alignment depends on the balance between this randomizing effect and the coupling between the NRs and the externally applied electric field. To quantify the NR alignment, extinction spectra are collected across a range of applied electric field strengths. A scalar order parameter S is then extracted from the spectra,⁴⁵ with an example shown in [Supporting Information Figure S1](#). The value of S is seen to increase from 0 for a randomly oriented suspension to a value of nearly 1 when the maximum field strength is applied, signifying that the NRs are largely oriented along the direction of light propagation (see [Supporting Information Figure S1b](#)).

For the low-frequency alternating current (AC) electric fields (60 Hz) applied in [Figures 1](#) and [2](#), the rotational diffusion time is less than the period of the applied field, therefore the NRs have sufficient time to randomize during each cycle.⁴⁶ When the period of the driving frequency is faster than the rotational diffusion time, the NRs remain aligned in the applied field direction.⁴⁶ The polymer coating of the NRs

has also been shown to significantly increase the rotational diffusion time due to hydrodynamic drag effects.^{46,55}

The critical electric field strength that is necessary to overcome randomizing influences in order to align the NRs theoretically depends on the NR volume and anisotropy.⁴⁵ The longer, higher-aspect-ratio NRs are therefore expected to require a smaller magnitude of the electric field to align. By collecting and analyzing field-dependent extinction spectra of each NR type, the critical electric field for alignment of each NR type is extracted, and it is confirmed that the critical electric field decreases from 1.9 to 0.22 V/ μ m for longer NRs as anticipated (see [Supporting Information Figure S2](#)).

The switching time of these materials is the sum of their on- and off-times. Under a strong electric field approximation, the randomization due to Brownian motion can be neglected, and the on-time becomes

$$\tau_{\text{on}} = \frac{\pi k_b T}{4D\Delta\alpha\epsilon_0 E^2} \quad (1)$$

and when the electric field is removed the off-time is

$$\tau_{\text{off}} = \frac{1}{6D} \quad (2)$$

where k_b is the Boltzmann constant, T is the absolute temperature, $\Delta\alpha = \alpha_{\parallel} - \alpha_{\perp}$ is the anisotropy of the NR polarizability, ϵ_0 is the permittivity of free space, E is the applied electric field, and the rotational diffusion coefficient, D , is

$$D = \frac{3k_b T}{\pi\eta L^3} \left(-\frac{0.05}{\text{AR}} + \frac{0.917}{\text{AR}} + \ln(\text{AR}) - 0.662 \right) \quad (3)$$

where L and AR are the NR's length and aspect ratio, respectively, and η is the host medium viscosity. The on-time is therefore predominantly set by the magnitude of the field applied, and the off-time is set by the rotational diffusion coefficient, yielding characteristic switching times on the order of 10s of microseconds.⁴⁶ Submicrosecond switching times have been achieved using nonplanar dynamic plasmonic pixels.⁴⁷

The use of AC electric fields and nonpolar solvents is critical to enable alignment.⁴⁵ Experiments carried out using direct current (DC) electric fields did not produce NR alignment, presumably due to charge screening effects. If the NRs were dispersed in polar, high-dielectric-constant solvents such as water and methanol, then NR alignment also did not occur, whereas nonpolar, low-dielectric-constant solvents have been shown to be effective hosts for alignment of metal NRs. The influence of the type of solvent on the alignment behavior is complex and includes considerations such as the contrast between the solvent and NR dielectric constants,^{56–58} the effect of the electric double layer at the NR–solvent interface,^{58–60} charge accumulation at the electrodes,^{58,59} and ionic impurity mobility,⁵⁹ many of which are frequency-dependent factors. Applying a uniform electric field across the suspension is also important to minimize the potential translational redistribution of NRs that would arise due to dielectrophoresis in a non-uniform field.^{49,51}

In addition to the wavelength tunability afforded by the choice of the NR geometry, the plasmon resonance spectrum can also be engineered by modifying the chemical composition of the NRs. In particular, the resonance of bimetallic nanostructures (either alloys or core–shell structures) can be

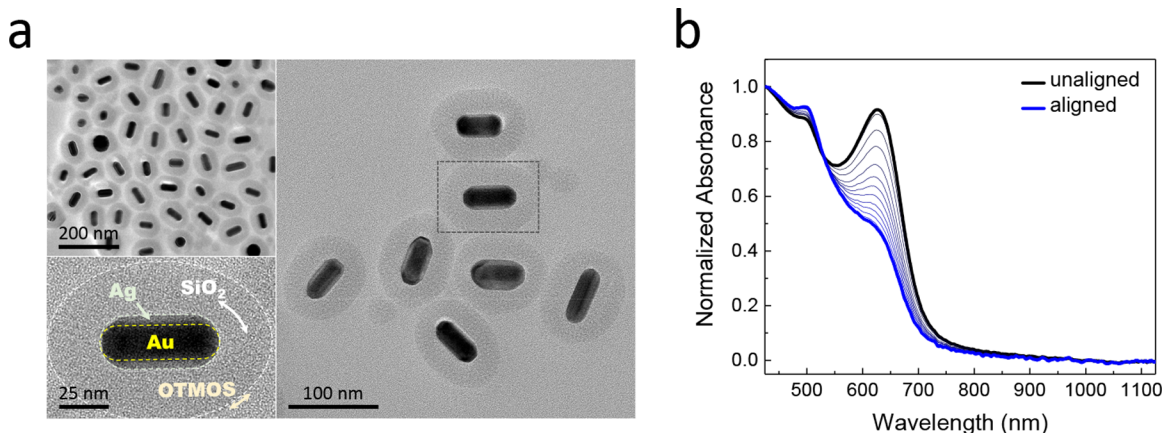


Figure 3. (a) Low-, medium-, and high-magnification TEM images of Au@Ag@SiO₂@OTMOS NRs. The enlarged, lower-left, annotated image corresponds to the region outlined in the image on the right. (b) Experimental modulation of the extinction spectrum of Au@Ag@SiO₂@OTMOS NRs in heptane upon alignment through application of external 60 Hz AC electric fields of varying strength (0–6 V/μm).

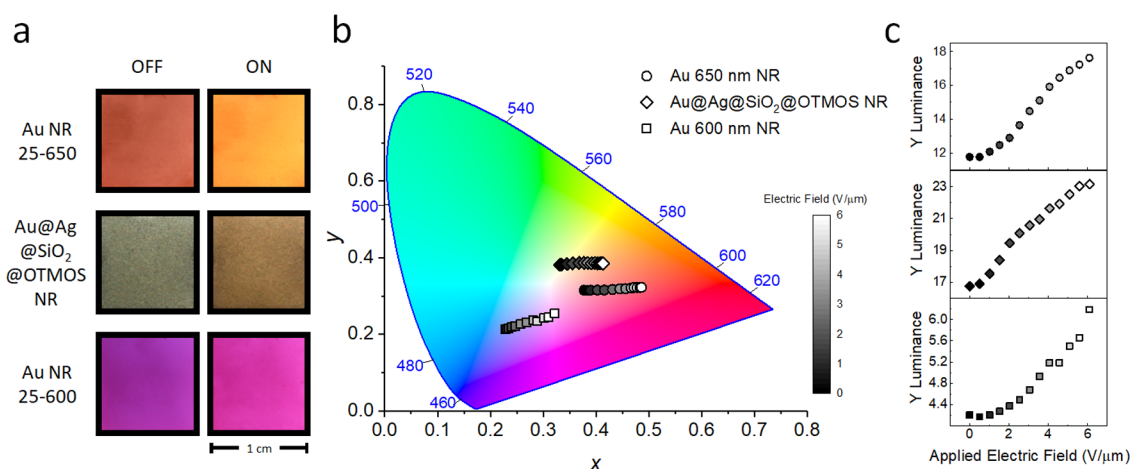


Figure 4. (a) Color photographs of the indicated NR suspensions (illuminated from the back by white light from a Xe lamp passing through a ground glass diffuser) when an applied 60 Hz AC electric field is either OFF (0 V/μm) or ON (6 V/μm). The properties of the Au NRs in toluene are labeled as “diameter-LSP” (nm), that is, “25–650” and “25–600.” The Au@Ag@SiO₂@OTMOS NRs are suspended in heptane. The NRs are contained in a custom-fabricated cell with an optical path of 0.2 mm and lateral dimension of 1 cm. (b) CIE 1931 x,y chromaticity coordinates and (c) luminance values (Y) plotted as a function of applied electric field for the three different NR suspensions. The xyY values are calculated from the spectra of Figures 2d and 3b.

tuned to an intermediate state between those of the two monometallic resonances.^{61–64} Here, in order to blue-shift the resonances of the Au NRs of Figure 2 to access additional regions of the visible spectrum, we formulated a core–shell NR structure through the overgrowth of Ag. To stabilize the Ag coating against the immediate chemical degradation after synthesis and enable dispersion in nonpolar solvents,^{65,66} the Au@Ag NRs were coated with a mesoporous SiO₂ shell. Next, by functionalizing the Au@Ag@SiO₂ NRs with alkyl-silane (octadecyltrimethoxysilane, OTMOS), the Au@Ag@SiO₂@OTMOS NRs were stable in nonpolar solvents such as heptane.

TEM images of the synthesized Au@Ag@SiO₂@OTMOS NRs are presented in Figure 3a. The images indicate distinct, and generally conformal, layers of Ag and SiO₂ around the central Au NR cores. The thickness of the Ag and SiO₂ layers along the sides of the NRs is estimated from the TEM images to be 3.9 ± 2.3 and 27 ± 3 nm, respectively. While there is some variation in the morphology, the Ag coating is generally thicker and easier to distinguish along the sides of the Au NR core than at the ends, as seen in the high-magnification image

of Figure 3a. When an external AC electric field is applied to the Au@Ag@SiO₂@OTMOS NRs under the same conditions described above for the Au NRs, the Au@Ag@SiO₂@OTMOS NRs align in the field direction, though with a spectral profile that is intentionally modified due to the presence of the Ag and SiO₂ coatings.

To better understand the changes in the spectra induced by the coatings, we simulated the spectra of Au@Ag NRs with increasing Ag shell thicknesses. Increasing the Ag thickness results in a greater blue-shift of the longitudinal plasmon resonance (see Supporting Information Figure S3a). For the experimentally determined Ag thickness of ~ 4 nm, the simulations predicted a blue-shift of ~ 70 nm, comparable to the ~ 50 nm blue-shift observed experimentally. While the simulated spectra do show heightened extinction below 500 nm when comparing the Au@Ag to the pure Au NRs, the effect is more dramatic in the experimental spectrum. This may be attributed to the presence of Ag impurities in the experimentally prepared sample that have plasmon resonances at < 500 nm. Simulation of the addition of a SiO₂ shell and suspension in methanol (Supporting Information Figure S3b)

indicates a red-shift of the longitudinal resonance of ~ 35 nm, due to the larger refractive index of the surrounding SiO_2 in comparison to the environment of the bare Au@Ag NRs. The magnitude of this shift is somewhat larger than the 5 nm shift observed in the experimental NR samples. This may be attributed to the experimental SiO_2 shell being mesoporous and therefore potentially having a lower refractive index than the bulk SiO_2 value used in the simulation. Based on reports by Tracy and colleagues^{67,68} that the refractive index of mesoporous SiO_2 is expected to be between 1.33 and 1.45, we simulate the extinction spectra of Au@Ag@ SiO_2 NRs over this range (see Supporting Information Figure S3c) and find that using a value of $n = 1.35$ most closely matches the experimental red-shift. The simulations in Supporting Information Figure S3d summarize the spectral evolution as the layers of the Au@Ag@ SiO_2 NRs are added: a substantial blue-shift upon adding the Ag, followed by small red-shifts upon adding the SiO_2 and upon dispersing in heptane ($n = 1.39$).

The alignment of NRs chosen from the library of Au and Au@Ag@ SiO_2 @OTMOS NRs described above provides a platform to display and modulate color across a significant portion of the visible spectrum. To demonstrate, Figure 4a presents color photographs of three different NR suspensions in unaligned (OFF) and aligned (ON) states. Backlit by a white light illuminant, each of the NR suspensions transmits a different distribution of visible light wavelengths as shown in their extinction spectra above. When the NRs are aligned, the resulting modulation of the spectrum is manifested as a distinct change in the observed color and brightness of the light passing through the NR suspension.

The color rendering properties of the NRs are quantified by mapping the NR spectra to International Commission on Illumination (CIE) 1931 xyY chromaticity and luminance values.⁶⁹ In general terms, the chromaticity coordinates x, y describe the “type” of color (e.g., red, green, blue), and the luminance Y indicates the brightness. The chromaticity diagram in Figure 4b illustrates that each of the three NR varieties modulates light over a different region of chromaticity. In each case, when the LSP mode is suppressed upon alignment, more red light is transmitted through the NR suspensions, and the chromaticity moves toward the red region of the diagram. The greater transmission of light is further exhibited as an increase in luminance, as seen in Figure 4c. The combination of the modified chromaticity and luminance generates the color change viewed by an observer. Because the different NR varieties operate over different regions of chromaticity, subpixels of each NR type can be envisioned to operate in tandem to constitute a trichromatic color mixing scheme⁷⁰ that renders a wider gamut than for an individual pixel.

To evaluate how well the experimentally characterized NRs perform in comparison to an idealized case, we simulated the spectra of unaligned and aligned NR suspensions of the three types presented in Figure 4 (see Supporting Information Figure S4). The experimental and simulated spectra show similar modulation behavior, though a noticeable difference is that in the simulations, the LSP peak is completely extinguished upon alignment. By contrast, in the experiments there is some residual LSP absorption even when the NRs are nearly fully aligned (see Supporting Information Figures S1 and S2). The simulations suggest that a large extinction contrast ratio, for example, $\sim 140:1$ for unaligned:aligned at the LSP peak for the 25–650 (diameter–LSP) Au NRs in Figure

4, can be achieved if a sufficiently large electric field is applied for complete alignment. There were two experimental contributions as to why the LSP absorption peak was nonzero when the NRs were fully aligned, for example, Figure 1b. First, the light was focused through the pixel using a lens, leading to a small solid angle of light incident onto the fully aligned NRs, thereby giving rise to a small amount of absorption from the LSP peak. Additionally, the low frequency of the AC electric fields (60 Hz) allowed the NRs to have sufficient time to unalign during each cycle, leading to additional absorption at the LSP wavelength. In future experiments, if collimated light is used to probe the pixels in conjunction with higher-frequency electric fields, then a contrast ratio closer to simulation values may be experimentally achievable. Another deviation from the simulations is the presence of non-NR impurities in the experimental spectra, whose extinction overlaps with and adds to the measured intensity in the region of the TSP peak. Finally, polydispersity in the synthesized NR dimensions leads to inhomogeneous broadening of the resonances.

The chromaticity modulation calculated from the simulated spectra is shown in Supporting Information Figure S5a. The three simulated NR types operate over similar chromaticity regions as those observed in the experimental results of Figure 4b. The chromaticities of the unaligned Au NR 25–600 and Au NR 25–650 originate at different locations but in the simulations converge to very similar values upon complete alignment since the TSP resonances are at similar wavelengths. However, the modulation of the chromaticity for the Au NR 25–600 is notably less in the experiments due to the incomplete NR alignment discussed above. The Au@Ag@ SiO_2 @OTMOS NRs modulate over a chromaticity region distinct from that of either of the pure Au NRs due to the blue-shift introduced by the Ag coating.

The absorbance of a NR suspension depends linearly on the concentration, which implies that pixels prepared with different NR concentrations would exhibit different luminance and chromaticity values. To explore this relationship further, we prepare a series of NR suspensions with different concentrations and map their spectra to xyY values. Supporting Information Figure S6a,b presents the experimentally measured spectra, expressed as both absorbance and transmittance. To expand the range of concentrations in the analysis beyond what could be directly measured without distortion by the spectrometer, extrapolated spectra are generated by following the linear relationship between absorbance and concentration determined in Supporting Information Figure S6c. From the experimental and extrapolated transmittance spectra, the dependences of luminance and chromaticity on concentration are illustrated in Supporting Information Figure S6d,e. At low concentration, where the transmittance is high for all wavelengths of illumination, the luminance is high and the chromaticity is near the white-point. Increasing the concentration lowers the transmittance at the plasmon resonance wavelengths, decreasing the luminance but shifting the chromaticity outward into the blue region of the diagram. The specifications desired for a given application therefore will necessitate choices on how to optimize the interrelation of NR concentration, chromaticity, and luminance. The optical path length (determined by the cell thickness) plays a similar role to NR concentration in determining the transmittance through the pixel. Representative photographs of NR suspensions of

different concentrations are provided in [Supporting Information Figure S6f](#).

To further demonstrate the potential implementation in display applications, we fabricated a seven-segment numerical indicator, shown in [Figure 5](#). Individually addressable electro-

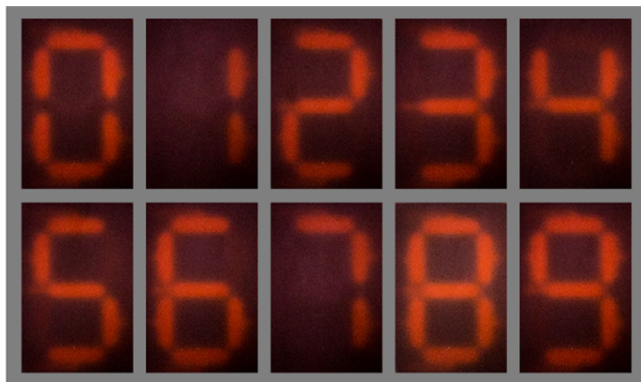


Figure 5. Composite of photographs of a fabricated seven-segment numerical indicator containing polystyrene-thiol-coated Au NRs in toluene. The indicator displays the numerals 0–9 as a 5 kHz electric field is applied across appropriate combinations of individually addressable, patterned electrodes. The outer dimensions of the "0" are 12.5 × 22 mm.

des patterned in indium tin oxide (ITO) on glass (see [Supporting Information Figure S7](#)) allow independent switching of each of the segments that constitute the numerals. Au NRs are dispersed throughout the entire volume between the glass plates. The contrast in luminance and chromaticity between segments to which an electric field is applied (which appear bright) and regions without an applied field (which appear dark) enables a clear rendering of each numeral. The functionality of the numerical indicator emphasizes the spatial, temporal, and spectral control conferred through the integration of switchable plasmonic NR materials within a larger device architecture.

CONCLUSIONS

By demonstrating the operation of plasmonic pixels throughout the visible and infrared spectral domains, we highlight the versatility of plasmonic NRs for high-speed optical applications. The NR spectrum is engineered both geometrically (through tailoring NR aspect ratio) and chemically (by overgrowth of Ag within a protective SiO₂ shell). We design NRs with a range of visible light chromaticities suited for color displays. Our fabrication of a plasmonic NR seven-segment indicator showcases that the NR materials are readily integrated into functional devices. Taking advantage of the highly parallel colloidal synthesis of NRs may confer a significant advantage over the costly, top-down processing often required for metasurface preparation. In contrast to conventional liquid crystal displays where half of the illumination intensity is automatically lost through polarization,⁷¹ the plasmonic pixel implementation shown here does not require polarized illumination, potentially bestowing enhanced energy efficiency. We envision the plasmonic NR pixel not only in display applications but also as a generic spatial light modulation platform for arbitrarily controlling the phase, amplitude, and polarization of light on a fast time scale.

METHODS

Preparation of Au NR Suspensions. Au NRs with longitudinal plasmon resonances in water at 600, 650, 700, 808, 900, and 1400 nm were acquired commercially (Nanopartz, Inc. #A12-25-600, A12-25-650, A12-25-700, A12-25-808, A12-25-900, and A12-25-1400). Au NRs with longitudinal resonances at 1100 nm in water were prepared using a modified seedless growth method (detailed in the [Supporting Information](#)). The highest-aspect-ratio Au NRs were prepared following the procedure of Khanal and Zubarev.⁷²

Purification and Phase Transfer of Au NR Suspensions. A detailed description is provided in the [Supporting Information](#). Briefly, excess surfactant was first removed from the as-prepared Au NR suspensions by centrifugation. Then, the Au NRs were phase transferred to toluene by functionalizing the NRs with thiol-terminated polystyrene (PS-thiol).⁴⁵ The Au NRs were then purified from excess, unbound PS-thiol by centrifugation.

Preparation of Au@Ag@SiO₂ NR. Au NR cores were prepared based on the methods of Park *et al.*⁷³ The Au NR cores were then coated with Ag using AgNO₃ along with ascorbic acid and NaOH, following a method based on that described by Park *et al.*⁷⁴ The Au@Ag NRs were overcoated with SiO₂ using a tetraethyl orthosilicate (TEOS) precursor, following a method adapted from Wu and Tracy.⁶⁸ Full details are provided in the [Supporting Information](#).

Phase Transfer of Au@Ag@SiO₂ NRs to Nonpolar Solvents. In order to make the Au@Ag@SiO₂ NRs stable in nonpolar solvents, the SiO₂ surface was functionalized with OTMOS, utilizing a method adapted from the report of Pastoriza-Santos *et al.*⁷⁵ and described in detail in the [Supporting Information](#). Following functionalization, the NRs were redispersed in heptane. A photograph of the phase transfer is presented in [Supporting Information Figure S8](#).

Transmission Electron Microscopy. Transmission electron microscopy was performed using a JEOL JEM-2200FS field emission electron microscope operating at 200 kV accelerating voltage. Samples were prepared by drop-casting NR suspensions onto holey-carbon-coated TEM grids (SPI Supplies, Structure Probe, Inc.).

Characterization of NR Alignment. To collect spectra of NRs aligned under an applied electric field, the NR suspensions were first loaded into rectangular capillaries (borosilicate glass extra wide microslide, path 0.20 mm, width 4.0 mm, wall 0.15 mm, length 50 mm; Glass Dynamics, L.L.C.). Each capillary was sealed with ultraviolet-light-curing adhesive (Norland Optical Adhesive 72). For measurement, a capillary was inserted in a home-built mount consisting of two inward-facing ITO-coated glass squares epoxied together with a gap of ~0.5 mm. Electrical leads were connected to the ITO using indium wire (Sigma-Aldrich) as solder, and the soldered connections were encapsulated with epoxy for added mechanical robustness. To prevent dielectric breakdown, the mount was immersed in silicone transformer oil (STO-50, Clearco Products Co., Inc.) contained within a transparent glass vessel with flat, parallel sides. A photograph of the experimental apparatus is provided in [Supporting Information Figure S9](#). A 60 Hz AC electric field was applied across the capillary by a high-voltage transformer (France, 1S030 PSG-2E) controlled by a variable autotransformer (3PN1010, Staco Energy Products Co.). The applied voltage was measured with a high-voltage probe (Fluke 80K-40 probe on a Fluke 73 Series II multimeter), and the magnitude of the electric field was estimated by dividing the voltage by the electrode separation distance. We have not explicitly taken into account the reduction of the field strength introduced by the presence of the capillary walls. For visible and near-infrared spectra, light from a halogen lamp (Ocean Optics HL-2000, 24 V) conveyed by an optical fiber was focused by a lens onto the NR suspension within the capillary. The transmitted light was collected by another lens and routed by an optical fiber to a spectrometer (Ocean Optics QEPro). To extend the measurable spectral range into the infrared for characterization of the high-aspect-ratio Au NRs, a dual-detector configuration was constructed using the external port of a Bruker Vertex 70 V Fourier-transform infrared (FTIR) spectrometer. Light from the halogen source of the FTIR was focused through the sample and then directed using a 50/50 beam splitter into both the

FTIR external mercury cadmium telluride IR detector and the Ocean Optics QEPro visible-light detector.

To account for any temporal variations in NR concentration within the collection region during the experiments, the spectra were normalized for comparison by the absorbance at 425 nm, where extinction is due to interband transitions rather than either the transverse or longitudinal plasmon resonances. A LOWESS smoothing algorithm was applied in OriginPro to reduce noise in the spectra, including fine absorption artifacts at 1696 and 1745 nm. To determine the CIE colorimetric values from the experimental spectra, the spectra were converted from absorbance units to transmittance and then loaded into the color math module of Ocean Optics' OceanView software. The xyY chromaticity and luminance coordinates were calculated using a D65 illuminant with 1 nm resolution and a 2° observer.

Photographs of 1 cm plasmonic pixels (Figure 4a) and the seven-segment numerical indicator (Figure 5) were obtained with a Canon EOS Rebel T3i digital camera and EF-S 18–55 mm lens at a focal length of 55 mm. A “daylight” in-camera white balance setting was used. Light from a Xe source (Oriel Instruments 68806) passing through a ground glass diffuser (Thorlabs) was used to back illuminate the samples.

In addition to using the 60 Hz voltage source described above, experiments were also carried out using a 5 kHz source. The terminals of a high-voltage ignition coil (MSD Blaster 2 8202) were connected to the NR alignment cell. Voltage was controlled with a custom-built electronic circuit implementing an IRF 520 N-channel MOSFET, a function generator (Stanford Research Systems DS340) providing a 5 kHz sine wave ($10 \text{ V}_{\text{p-p}}$, 5 V_{DC} offset) and a DC power supply (Leader LPS-152). The applied voltage signal ($\sim 11 \text{ kV}_{\text{p-p}}$) was monitored using a Tektronix P6015A high-voltage probe connected to a Tektronix TDS1002 digital oscilloscope. While the appearance to the human eye of the aligned NR suspensions was similar between the 60 Hz and 5 kHz sources, the 5 kHz source was favorable for photographic imaging because the higher frequency enabled, for example, the capture of 30 frame/s video without flicker from the modulation of the voltage source.

Fabrication of Seven-Segment Numerical Indicator and Single-Pixel Cells. The seven-segment (Figure 5) and single-pixel (Figure 4 a) displays were fabricated using a combination of laser micromachining and standard photolithographic techniques. ITO-coated glass plates ($50 \times 75 \times 0.7 \text{ mm}$) were laser micromachined to isolate each segment of the display using an Nd:YVO₄ diode-pumped laser (JDSU, Q301-HD, $\lambda = 355 \text{ nm}$, 30 ns). After patterning, the ITO was coated with a dielectric layer (Microchem, SU8), and a spacer was laser-cut (Kapton, 8 mils) to form the liquid reservoir. The ITO plates and middle spacer were then bonded together using a UV-curable adhesive (Norland, NOA72). The leads for electrical connection were then attached with silver epoxy. The NR suspensions were injected into the liquid reservoir with a micropipette, where the suspension was evenly distributed by capillary wetting.

Simulations. Simulations were performed using the commercial finite-element simulation software COMSOL Multiphysics.⁷⁶ Additional details are provided in the Supporting Information.

ASSOCIATED CONTENT

Supporting Information

The Supporting Information is available free of charge on the ACS Publications website at DOI: [10.1021/acsnano.9b00905](https://doi.org/10.1021/acsnano.9b00905).

Description of additional experimental and simulation details. Extinction spectra and extracted orientational order parameter as a function of applied electric field strength. Critical electric field for alignment for Au NRs of different aspect ratios. Simulations of the modification to the spectrum of Au NRs upon overgrowth of Ag and SiO₂. Simulated modulation of extinction spectra upon alignment and resulting chromaticity modulation. Effect of NR concentration on luminance and chromaticity.

Schematic diagrams of seven-segment numerical indicator. Photographs of NR phase transfer and experimental apparatus ([PDF](#))

AUTHOR INFORMATION

Corresponding Author

*E-mail: jake.fontana@nrl.navy.mil.

ORCID ®

Kristin Charipar: [0000-0002-5870-0945](#)

Paul Johns: [0000-0002-1134-7566](#)

Kyoungweon Park: [0000-0001-8069-3000](#)

Richard A. Vaia: [0000-0003-4589-3423](#)

Jake Fontana: [0000-0002-3732-942X](#)

Funding

This material is based in part upon work supported by the Office of Naval Research under (N0001418WX00122).

Notes

The authors declare no competing financial interest.

ACKNOWLEDGMENTS

N.J.G. thanks the NRC for a postdoctoral fellowship. P.J. and J.A.G. thank the ASEE for postdoctoral fellowships. S.J.B. thanks the ASEE for a graduate internship as well as J. Herzog with the University of Arkansas and University of Indianapolis for the support of computational work. The authors thank J. Kolacz, H. Gotjen, J. Russell, and R. Suess for helpful discussions and use of equipment and M. Chiriboga for assistance with TEM imaging.

REFERENCES

- (1) Borshch, V.; Shiyanskii, S. V.; Lavrentovich, O. D. Nano-second Electro-Optic Switching of a Liquid Crystal. *Phys. Rev. Lett.* **2013**, *111*, 107802.
- (2) Someya, J.; Sugiura, H. Evaluation of Liquid-Crystal-Display Motion Blur with Moving-Picture Response Time and Human Perception. *J. Soc. Inf. Disp.* **2007**, *15*, 79–86.
- (3) Ghodrati, M.; Morris, A. P.; Price, N. S. The (Un)Suitability of Modern Liquid Crystal Displays (LCDs) for Vision Research. *Front. Psychol.* **2015**, *6*, 303.
- (4) Kristensen, A.; Yang, J. K. W.; Bozhevolnyi, S. I.; Link, S.; Nordlander, P.; Halas, N. J.; Mortensen, N. A. Plasmonic Colour Generation. *Nat. Rev. Mater.* **2017**, *2*, 16088.
- (5) Keshavarz Hedayati, M.; Elbahri, M. Review of Metasurface Plasmonic Structural Color. *Plasmonics* **2017**, *12*, 1463–1479.
- (6) Zhao, Y.; Zhao, Y.; Hu, S.; Lv, J.; Ying, Y.; Gervinskas, G.; Si, G. Artificial Structural Color Pixels: A Review. *Materials* **2017**, *10*, 944.
- (7) Shao, L.; Zhuo, X.; Wang, J. Advanced Plasmonic Materials for Dynamic Color Display. *Adv. Mater.* **2018**, *30*, 1704338.
- (8) Kim, I.; Yoon, G.; Jang, J.; Genevet, P.; Nam, K. T.; Rho, J. Outfitting Next Generation Displays with Optical Metasurfaces. *ACS Photonics* **2018**, *5*, 3876–3895.
- (9) Xu, T.; Wu, Y. K.; Luo, X.; Guo, L. J. Plasmonic Nanoresonators for High-Resolution Colour Filtering and Spectral Imaging. *Nat. Commun.* **2010**, *1*, 59.
- (10) Kumar, K.; Duan, H.; Hegde, R. S.; Koh, S. C.; Wei, J. N.; Yang, J. K. Printing Colour at the Optical Diffraction Limit. *Nat. Nanotechnol.* **2012**, *7*, 557–561.
- (11) Roberts, A. S.; Pors, A.; Albrektsen, O.; Bozhevolnyi, S. I. Subwavelength Plasmonic Color Printing Protected for Ambient Use. *Nano Lett.* **2014**, *14*, 783–787.
- (12) Shrestha, V. R.; Lee, S. S.; Kim, E. S.; Choi, D. Y. Aluminum Plasmonics Based Highly Transmissive Polarization-Independent Subtractive Color Filters Exploiting a Nanopatch Array. *Nano Lett.* **2014**, *14*, 6672–6678.

- (13) Olson, J.; Manjavacas, A.; Liu, L.; Chang, W. S.; Foerster, B.; King, N. S.; Knight, M. W.; Nordlander, P.; Halas, N. J.; Link, S. Vivid, Full-Color Aluminum Plasmonic Pixels. *Proc. Natl. Acad. Sci. U. S. A.* **2014**, *111*, 14348–14353.
- (14) Rajasekharan, R.; Balaur, E.; Minovich, A.; Collins, S.; James, T. D.; Djalalian-Assl, A.; Ganesan, K.; Tomljenovic-Hanic, S.; Kandasamy, S.; Skafidas, E.; Neshev, D. N.; Mulvaney, P.; Roberts, A.; Prawer, S. Filling Schemes at Submicron Scale: Development of Submicron Sized Plasmonic Colour Filters. *Sci. Rep.* **2015**, *4*, 6435.
- (15) Tan, S. J.; Zhang, L.; Zhu, D.; Goh, X. M.; Wang, Y. M.; Kumar, K.; Qiu, C. W.; Yang, J. K. Plasmonic Color Palettes for Photorealistic Printing with Aluminum Nanostructures. *Nano Lett.* **2014**, *14*, 4023–4029.
- (16) Goh, X. M.; Zheng, Y.; Tan, S. J.; Zhang, L.; Kumar, K.; Qiu, C. W.; Yang, J. K. Three-Dimensional Plasmonic Stereoscopic Prints in Full Colour. *Nat. Commun.* **2014**, *5*, 5361.
- (17) Duempelmann, L.; Casari, D.; Luu-Dinh, A.; Gallinet, B.; Novotny, L. Color Rendering Plasmonic Aluminum Substrates with Angular Symmetry Breaking. *ACS Nano* **2015**, *9*, 12383–12391.
- (18) Miyata, M.; Hatada, H.; Takahara, J. Full-Color Subwavelength Printing with Gap-Plasmonic Optical Antennas. *Nano Lett.* **2016**, *16*, 3166–3172.
- (19) Zhu, X.; Vannahme, C.; Hojlund-Nielsen, E.; Mortensen, N. A.; Kristensen, A. Plasmonic Colour Laser Printing. *Nat. Nanotechnol.* **2016**, *11*, 325–329.
- (20) James, T. D.; Mulvaney, P.; Roberts, A. The Plasmonic Pixel: Large Area, Wide Gamut Color Reproduction Using Aluminum Nanostructures. *Nano Lett.* **2016**, *16*, 3817–3823.
- (21) Wang, L.; Ng, R. J. H.; Safari Dinachali, S.; Jalali, M.; Yu, Y.; Yang, J. K. W. Large Area Plasmonic Color Palettes with Expanded Gamut Using Colloidal Self-Assembly. *ACS Photonics* **2016**, *3*, 627–633.
- (22) Li, Z.; Clark, A. W.; Cooper, J. M. Dual Color Plasmonic Pixels Create a Polarization Controlled Nano Color Palette. *ACS Nano* **2016**, *10*, 492–498.
- (23) Balaur, E.; Sadatnajafi, C.; Kou, S. S.; Lin, J.; Abbey, B. Continuously Tunable, Polarization Controlled, Colour Palette Produced from Nanoscale Plasmonic Pixels. *Sci. Rep.* **2016**, *6*, 28062.
- (24) Goh, X. M.; Ng, R. J. H.; Wang, S.; Tan, S. J.; Yang, J. K. W. Comparative Study of Plasmonic Colors from All-Metal Structures of Posts and Pits. *ACS Photonics* **2016**, *3*, 1000–1009.
- (25) Wang, H.; Wang, X.; Yan, C.; Zhao, H.; Zhang, J.; Santschi, C.; Martin, O. J. F. Full Color Generation Using Silver Tandem Nanodisks. *ACS Nano* **2017**, *11*, 4419–4427.
- (26) Heydari, E.; Sperling, J. R.; Neale, S. L.; Clark, A. W. Plasmonic Color Filters as Dual-State Nanopixels for High-Density Microimage Encoding. *Adv. Funct. Mater.* **2017**, *27*, 1701866.
- (27) Jiang, N.; Zhuo, X.; Wang, J. Active Plasmonics: Principles, Structures, and Applications. *Chem. Rev.* **2018**, *118*, 3054–3099.
- (28) Liu, Y. J.; Si, G. Y.; Leong, E. S.; Xiang, N.; Danner, A. J.; Teng, J. H. Light-Driven Plasmonic Color Filters by Overlaying Photoresponsive Liquid Crystals on Gold Annular Aperture Arrays. *Adv. Mater.* **2012**, *24*, OP131–OP135.
- (29) Franklin, D.; Chen, Y.; Vazquez-Guardado, A.; Modak, S.; Boroumand, J.; Xu, D.; Wu, S. T.; Chanda, D. Polarization-Independent Actively Tunable Colour Generation on Imprinted Plasmonic Surfaces. *Nat. Commun.* **2015**, *6*, 7337.
- (30) Franklin, D.; Frank, R.; Wu, S. T.; Chanda, D. Actively Addressed Single Pixel Full-Colour Plasmonic Display. *Nat. Commun.* **2017**, *8*, 15209.
- (31) Miyata, M.; Kaijima, A.; Nagasaki, Y.; Takahara, J. Electro-mechanically Tunable Plasmonic Nanowires Operating in Visible Wavelengths. *ACS Photonics* **2016**, *3*, 2268–2274.
- (32) Zhang, M.; Magagnosc, D. J.; Liberal, I.; Yu, Y.; Yun, H.; Yang, H.; Wu, Y.; Guo, J.; Chen, W.; Shin, Y. J.; Stein, A.; Kikkawa, J. M.; Engheta, N.; Gianola, D. S.; Murray, C. B.; Kagan, C. R. High-Strength Magnetically Switchable Plasmonic Nanorods Assembled from a Binary Nanocrystal Mixture. *Nat. Nanotechnol.* **2017**, *12*, 228–232.
- (33) Wang, M.; Gao, C.; He, L.; Lu, Q.; Zhang, J.; Tang, C.; Zorba, S.; Yin, Y. Magnetic Tuning of Plasmonic Excitation of Gold Nanorods. *J. Am. Chem. Soc.* **2013**, *135*, 15302–15305.
- (34) Xiong, K.; Emilsson, G.; Maziz, A.; Yang, X.; Shao, L.; Jager, E. W.; Dahlin, A. B. Plasmonic Metasurfaces with Conjugated Polymers for Flexible Electronic Paper in Color. *Adv. Mater.* **2016**, *28*, 9956–9960.
- (35) Xu, T.; Walter, E. C.; Agrawal, A.; Bohn, C.; Velmurugan, J.; Zhu, W.; Lezec, H. J.; Talin, A. A. High-Contrast and Fast Electrochromic Switching Enabled by Plasmonics. *Nat. Commun.* **2016**, *7*, 10479.
- (36) Lu, W.; Jiang, N.; Wang, J. Active Electrochemical Plasmonic Switching on Polyaniline-Coated Gold Nanocrystals. *Adv. Mater.* **2017**, *29*, 1604862.
- (37) Stec, G. J.; Lauchner, A.; Cui, Y.; Nordlander, P.; Halas, N. J. Multicolor Electrochromic Devices Based on Molecular Plasmonics. *ACS Nano* **2017**, *11*, 3254–3261.
- (38) Tsuboi, A.; Nakamura, K.; Kobayashi, N. A Localized Surface Plasmon Resonance-Based Multicolor Electrochromic Device with Electrochemically Size-Controlled Silver Nanoparticles. *Adv. Mater.* **2013**, *25*, 3197–3201.
- (39) Wang, G.; Chen, X.; Liu, S.; Wong, C.; Chu, S. Mechanical Chameleon through Dynamic Real-Time Plasmonic Tuning. *ACS Nano* **2016**, *10*, 1788–1794.
- (40) Byers, C. P.; Zhang, H.; Swearer, D. F.; Yorulmaz, M.; Hoener, B. S.; Huang, D.; Hoggard, A.; Chang, W. S.; Mulvaney, P.; Ringe, E.; Halas, N. J.; Nordlander, P.; Link, S.; Landes, C. F. From Tunable Core-Shell Nanoparticles to Plasmonic Drawbridges: Active Control of Nanoparticle Optical Properties. *Sci. Adv.* **2015**, *1*, No. e1500988.
- (41) Duan, X.; Kamin, S.; Liu, N. Dynamic Plasmonic Colour Display. *Nat. Commun.* **2017**, *8*, 14606.
- (42) Si, G.; Zhao, Y.; Leong, E. S. P.; Liu, Y. J. Liquid-Crystal-Enabled Active Plasmonics: A Review. *Materials* **2014**, *7*, 1296–1317.
- (43) Zhang, Y.; Liu, Q.; Mundoor, H.; Yuan, Y.; Smalyukh, II Metal Nanoparticle Dispersion, Alignment, and Assembly in Nematic Liquid Crystals for Applications in Switchable Plasmonic Color Filters and E-Polarizers. *ACS Nano* **2015**, *9*, 3097–3108.
- (44) Olson, J.; Manjavacas, A.; Basu, T.; Huang, D.; Schlather, A. E.; Zheng, B.; Halas, N. J.; Nordlander, P.; Link, S. High Chromaticity Aluminum Plasmonic Pixels for Active Liquid Crystal Displays. *ACS Nano* **2016**, *10*, 1108–1117.
- (45) Fontana, J.; da Costa, G. K. B.; Pereira, J. M.; Naciri, J.; Ratna, B. R.; Palffy-Muhoray, P.; Carvalho, I. C. S. Electric Field Induced Orientational Order of Gold Nanorods in Dilute Organic Suspensions. *Appl. Phys. Lett.* **2016**, *108*, 081904.
- (46) Etcheverry, S.; Araujo, L. F.; da Costa, G. K. B.; Pereira, J. M. B.; Camara, A. R.; Naciri, J.; Ratna, B. R.; Hernández-Romano, I.; de Matos, C. J. S.; Carvalho, I. C. S.; Margulis, W.; Fontana, J. Microsecond Switching of Plasmonic Nanorods in an All-Fiber Optofluidic Component. *Optica* **2017**, *4*, 864–870.
- (47) Etcheverry, S.; Araujo, L. F.; Carvalho, I. C. S.; Margulis, W.; Fontana, J. Digital Electric Field Induced Switching of Plasmonic Nanorods Using an Electro-Optic Fluid Fiber. *Appl. Phys. Lett.* **2017**, *111*, 221108.
- (48) van der Zande, B. M. I.; Koper, G. J. M.; Lekkerkerker, H. N. W. Alignment of Rod-Shaped Gold Particles by Electric Fields. *J. Phys. Chem. B* **1999**, *103*, 5754–5760.
- (49) Edwards, B.; Engheta, N.; Evoy, S. Theory of Simultaneous Control of Orientation and Translational Motion of Nanorods Using Positive Dielectrophoretic Forces. *J. Appl. Phys.* **2005**, *98*, 124314.
- (50) Fontana, J.; Palffy-Muhoray, P.; Kotov, N.; Agarwal, A. Measurements of the Electric Susceptibilities of Au Nanorods at Optical Frequencies. Proceedings from the American Physical Society March Meeting, March 10–14, 2008, New Orleans, LA; American Physical Society: College Park, MD, 2008.
- (51) Golovin, A. B.; Lavrentovich, O. D. Electrically Reconfigurable Optical Metamaterial Based on Colloidal Dispersion of Metal Nanorods in Dielectric Fluid. *Appl. Phys. Lett.* **2009**, *95*, 254104.

- (52) Ruda, H. E.; Shik, A. Nanorod Dynamics in AC Electric Fields. *Nanotechnology* **2010**, *21*, 235502.
- (53) Golovin, A.; Xiang, J.; Park, H.-S.; Tortora, L.; Nastishin, Y.; Shiyanovskii, S.; Lavrentovich, O. Electro-Optic Effects in Colloidal Dispersion of Metal Nano-Rods in Dielectric Fluid. *Materials* **2011**, *4*, 390–416.
- (54) Zheng, X.; Fontana, J.; Pevnyi, M.; Ignatenko, M.; Wang, S.; Vaia, R.; Palfy-Muhoray, P. The Effects of Nanoparticle Shape and Orientation on the Low Frequency Dielectric Properties of Nano-composites. *J. Mater. Sci.* **2012**, *47*, 4914–4920.
- (55) Zijlstra, P.; van Stee, M.; Verhart, N.; Gu, Z.; Orrit, M. Rotational Diffusion and Alignment of Short Gold Nanorods in an External Electric Field. *Phys. Chem. Chem. Phys.* **2012**, *14*, 4584–4588.
- (56) Ruda, H. E.; Shik, A. Principles of Nanowire Alignment in an Electric Field. *J. Appl. Phys.* **2011**, *109*, 064305.
- (57) Shik, A.; Ruda, H. E.; Currie, I. G. Electromechanical and Electro-Optical Properties of Nanowires. *J. Appl. Phys.* **2005**, *98*, 094306.
- (58) Dozov, I.; Paineau, E.; Davidson, P.; Antonova, K.; Baravian, C.; Biannic, I.; Michot, L. J. Electric-Field-Induced Perfect Anti-Nematic Order in Isotropic Aqueous Suspensions of a Natural Beidellite Clay. *J. Phys. Chem. B* **2011**, *115*, 7751–7765.
- (59) Buluy, O.; Aryasova, N.; Tereshchenko, O.; Kurioz, Y.; Nazarenko, V.; Eremin, A.; Stannarius, R.; Klein, S.; Goldmann, C.; Davidson, P.; Dozov, I.; Reznikov, Y. Optical and X-Ray Scattering Studies of the Electric Field-Induced Orientational Order in Colloidal Suspensions of Pigment Nanorods. *J. Mol. Liq.* **2018**, *267*, 286–296.
- (60) Arcenegui, J. J.; Garcia-Sanchez, P.; Morgan, H.; Ramos, A. Electro-Orientation of a Metal Nanowire Counterbalanced by Thermal Torques. *Phys. Rev. E* **2014**, *89*, 062306.
- (61) Rycenga, M.; Cobley, C. M.; Zeng, J.; Li, W.; Moran, C. H.; Zhang, Q.; Qin, D.; Xia, Y. Controlling the Synthesis and Assembly of Silver Nanostructures for Plasmonic Applications. *Chem. Rev.* **2011**, *111*, 3669–3712.
- (62) Jiang, R.; Chen, H.; Shao, L.; Li, Q.; Wang, J. Unraveling the Evolution and Nature of the Plasmons in (Au Core)-(Ag Shell) Nanorods. *Adv. Mater.* **2012**, *24*, OP200–OP207.
- (63) Motl, N. E.; Smith, A. F.; DeSantis, C. J.; Skrabalak, S. E. Engineering Plasmonic Metal Colloids through Composition and Structural Design. *Chem. Soc. Rev.* **2014**, *43*, 3823–3834.
- (64) Gilroy, K. D.; Ruditskiy, A.; Peng, H. C.; Qin, D.; Xia, Y. Bimetallic Nanocrystals: Syntheses, Properties, and Applications. *Chem. Rev.* **2016**, *116*, 10414–10472.
- (65) Ung, T.; Liz-Marzán, L. M.; Mulvaney, P. Controlled Method for Silica Coating of Silver Colloids. Influence of Coating on the Rate of Chemical Reactions. *Langmuir* **1998**, *14*, 3740–3748.
- (66) Hanske, C.; Sanz-Ortíz, M. N.; Liz-Marzan, L. M. Silica-Coated Plasmonic Metal Nanoparticles in Action. *Adv. Mater.* **2018**, *30*, 1707003.
- (67) Rowe, L. R.; Chapman, B. S.; Tracy, J. B. Understanding and Controlling the Morphology of Silica Shells on Gold Nanorods. *Chem. Mater.* **2018**, *30*, 6249–6258.
- (68) Wu, W. C.; Tracy, J. B. Large-Scale Silica Overcoating of Gold Nanorods with Tunable Shell Thicknesses. *Chem. Mater.* **2015**, *27*, 2888–2894.
- (69) Smith, T.; Guild, J. The C.I.E. Colorimetric Standards and Their Use. *Trans. Opt. Soc., London* **1932**, *33*, 73–134.
- (70) Rezaei, S. D.; Ho, J.; Ng, R. J. H.; Ramakrishna, S.; Yang, J. K. W. On the Correlation of Absorption Cross-Section with Plasmonic Color Generation. *Opt. Express* **2017**, *25*, 27652–27664.
- (71) Cornelissen, H. Polarized-Light Backlights for Liquid-Crystal Displays. *SPIE Newsroom* (online), 2008. <http://www.spie.org/newsroom/1363-polarized-light-backlights-for-liquid-crystal-displays?SSO=1> (accessed January 11, 2019).
- (72) Khanal, B. P.; Zubarev, E. R. Purification of High Aspect Ratio Gold Nanorods: Complete Removal of Platelets. *J. Am. Chem. Soc.* **2008**, *130*, 12634–12635.
- (73) Park, K.; Hsiao, M. S.; Yi, Y. J.; Izor, S.; Koerner, H.; Jawaid, A.; Vaia, R. A. Highly Concentrated Seed-Mediated Synthesis of Monodispersed Gold Nanorods. *ACS Appl. Mater. Interfaces* **2017**, *9*, 26363–26371.
- (74) Park, K.; Drummy, L. F.; Vaia, R. A. Ag Shell Morphology on Au Nanorod Core: Role of Ag Precursor Complex. *J. Mater. Chem.* **2011**, *21*, 15608–15618.
- (75) Pastoriza-Santos, I.; Pérez-Juste, J.; Liz-Marzán, L. M. Silica-Coating and Hydrophobation of CTAB-Stabilized Gold Nanorods. *Chem. Mater.* **2006**, *18*, 2465–2467.
- (76) COMSOL Multiphysics, v. 5.3a; COMSOL AB: Stockholm, Sweden, 2018.